Physica B 716 (2025) 417713

Contents lists available at ScienceDirect

Physica B: Condensed Matter

journal homepage: www.elsevier.com/locate/physb

Theoretical investigations on structural, electronic, elastic, thermal, optic and hydrogen storage properties of $XAlH_6$ (X= La, Ce, Pr) aluminium hydrides

Çağatay Yamçıçıer [a,*], Selgin Al [b], Cihan Kürkçü [c]

[a] Department of Electricity and Energy, Kadirli Vocational School, Osmaniye Korkut Ata University, Osmaniye, Türkiye
[b] Department of Environmental Protection Technologies, Vocational School, Izmir Democracy University, Izmir, Türkiye
[c] Department of Electronics and Automation, Kirsehir Ahi Evran University, Kırşehir, Türkiye

ARTICLE INFO

Keywords:
Hydrogen storage
Mechanical stability
Electronic properties
First principles

ABSTRACT

The structural, mechanical, electronic, thermodynamic, and hydrogen storage characteristics of trigonal $XAlH_6$ (X = La, Ce, and Pr) has been studied by using density functional theory which are not previously explored experimentally/computationally. Firstly, the equilibrium crystal structures, formation enthalpies for $XAlH_6$ (X = La, Ce, and Pr) are computed and assessed for synthesisability and thermodynamic stability of the materials. Subsequently, elastic constants of the materials were calculated and evaluated. The results indicated that $XAlH_6$ (X = La, Ce, and Pr) is mechanically, thermodynamically stable, and feasible for synthesis. The examination of bulk modulus to shear modulus ratio, Cauchy pressure, and Poisson's ratio displayed that $XAlH_6$ exhibits brittleness. The electronic band structure analyses demonstrate that there is a band gap of 2.05 eV and 0.95 eV between the maximum of the valence band and the minimum of the conduction band around the Fermi energy level for $LaAlH_6$ and $PrAlH_6$, respectively. Therefore, $LaAlH_6$ and $PrAlH_6$ have semiconducting properties. $CeAlH_6$ is found to be metallic because the bands cross the Fermi energy level. The optical properties are also investigated in depth. In the visible spectrum, electromagnetic radiation with a polarization of [1 0 0] has a reflectivity of less than 40 %, hence $XAlH_6$ can also be a good candidate as an anti-reflection material. The GDH (gravimetric hydrogen density) values are calculated to be 3.52 wt % for $LaAlH_6$, 3.50 wt % for $CeAlH_6$, and 3.48 wt % for $PrAlH_6$. Additionally, the hydrogen desorption temperatures are determined to be 292.28 K for $LaAlH_6$, 301.87 K for $CeAlH_6$, and 361.01 K for $PrAlH_6$. The findings suggest that these materials can be promising host for solid state hydrogen storage.

1. Introduction

Hydrogen is a promising energy source for the future due to its abundance, cleanness, light weight, high energy content per mass, and relatively ease of storage compared to electricity. One of the challenges for its common use to shift from carbon to zero carbon energy systems is storing hydrogen efficiently and safely. To satisfy the strict requirements of high energy density, reversibility, and operational safety, a variety of strategies have been investigated, such as liquid hydrogen, high-pressure gas storage, and solid-state storage in metal hydrides. The most conventional way of storing hydrogen is in gas form in highly pressurized cylinders. There are disadvantages associated with this approach since it requires high pressure tanks and has low density. However, research continues and offers solid state hydrogen storage which has garnered significant attention due to offering promising solutions to store hydrogen more efficiently and safely.

Because of their potential for reversible hydrogen absorption and desorption under mild conditions, metal hydrides have garnered a lot of study interest. Metal hydrides have been the subject of recent studies because of their high volumetric hydrogen density and mild reversibility. Development of aluminium-based hydrides, rare-earth metal hydrides, and perovskite-type hydrides is a potential strategy. Regarding the stability, reversibility, and hydrogen storage capacity, each group offers benefits and difficulties. Perovskite type hydrides such as $CaXH_3$ (where X = Mn, Fe, and Co) [1], $KCaH_3$ and $KSrH_3$ [2] and $LiCaH_3$ and $NaCaH_3$ [3] have been thoroughly investigated for their mechanical,

* Corresponding author.
E-mail address: cagatayyamcicier@osmaniye.edu.tr (Ç. Yamçıçıer).

https://doi.org/10.1016/j.physb.2025.417713
Received 18 June 2025; Received in revised form 4 August 2025; Accepted 18 August 2025
Available online 19 August 2025

structural, and hydrogen-storage capabilities using Density Functional Theory (DFT) calculations, these materials have hydrogen storage densities ranging from 2.28 to 5.70 wt%. Because of their improved thermodynamic tunability, they can now compete with traditional metal hydrides. Still, there are difficulties in maximizing their kinetic characteristics for quicker cycles of hydrogen absorption and desorption. $LiBH_4$'s high hydrogen capacity has made it a desirable option for hydrogen storage [4–7]. Through techniques such as doping and the use of catalysts, research has attempted to overcome its poor kinetics and thermodynamic stability. Research describes its structural characteristics, pressure-induced phase shifts, and decomposition reactions, particularly those that are catalysed. $LiBH_4$ has an orthorhombic structure, and by adding certain substances, its hydrogen desorption can be adjusted to lower the necessary temperatures.

Because of their comparatively high hydrogen storage capacities and lightweight nature, aluminium-based hydrides such as $LiAlH_4$ and $NaAlH_4$ have also attracted a lot of attention as possible hydrogen storage materials. For example, $LiAlH_4$ has the potential to store up to 9.5 wt % hydrogen [8]. The fact that these materials are naturally extremely stable and need high temperatures to liberate hydrogen is a major obstacle for end-user applications. Studies have demonstrated that these hydrides can release hydrogen more quickly by mechano-chemical processing in ambient settings, particularly when transition metal catalysts are present. Although the kinetics of hydrogen release have been improved, aluminium-based hydrides still have several drawbacks. To accomplish reversible hydrogen storage at reasonable temperatures (below 100 °C), they frequently need to be doped with additions such as titanium; even then, the reversible capacity is only about 3 wt%. Utilizing these materials is made more difficult and expensive by the intricate reaction processes and the requirement for catalysts. The crystal structure of $SrAlD_5$, a strontium-aluminium deuteride that is a member of the penta-alanate class of aluminium-based complex hydrides was determined [9]. The work illustrates how reducing cation size improves structural complexity and tilting of AlD_6 chains by contrasting $SrAlD_5$ with similar compounds such as $CaAlD_5$ and $BaAlD_5$ and proposed as promising hydrogen storage material. In an another study, hydrogen storage potential of two perovskite-type aluminium-based hydrides, $NaAlH_3$ and $MgAlH_3$, using DFT method was explored [10]. $NaAlH_3$ and $MgAlH_3$ are suggested as promising candidates for hydrogen storage, especially $NaAlH_3$ due to its higher hydrogen capacity and ductility. In a recent study, hydrogenation and dehydrogenation performance of non-stoichiometric $Li_xNa_{3-x}AlH_6$ compounds was carefully investigated [11], and the composition $Li_{1.3}Na_{1.7}AlH_6$ was shown to be the most notable. The samples that had the lowest beginning dehydrogenation temperature (423 K), which was more than 40 K lower than the others, and the maximum hydrogen capacity (3.45 wt%) were $Li_{1.3}Na_{1.7}AlH_6$. In comparison to $LiNa_2AlH_6$ (68.1 kJ mol^{-1} H_2), it also showed a considerable reduction in its dehydrogenation enthalpy to 49.7 kJ mol^{-1} H_2, suggesting higher thermodynamic instability. Among other hydrides, aluminium based hydrides are less investigated material class. To maximize the potential of hydrogen storage materials, it is essential to investigate various material classes, crystal structures, hydrogenation, electrical, elastic, anisotropic, and thermodynamic properties. Understanding a material's behaviour at practical hydrogen storage pressures and temperatures, for instance, can be facilitated by forecasting how it would react to pressure. As a result, the necessity to find new material classes is constant. Also, first-principles calculations explore advanced materials for hydrogen storage and hydrogen evolution reactions. Several studies focus on the structural stability, hydrogen storage capacity, dehydrogenation mechanisms, and physical properties of various hydrides, including novel phases of $KAlH_4$, $LiAlH_4$, and $AMMgH_3$ (AM = Li, Na, K, Rb) hydrides, as well as $B_3N_3H_6$-type $X_3N_3H_6$ (X = B, C, Al) hydrides, with calculated hydrogen storage capacities ranging from 2.68 wt% to 8.76 wt% and predictions of their electronic and optical properties [12–17].

Accordingly, this study uses density functional theory simulations to examine the structural, elastic, isotropic, electrical, optical, dynamic, and thermodynamic features of the rare-earth metal aluminium hydrides $XAlH_6$ (X = La, Ce, Pr). A detailed discussion is given of a number of parameters derived from elastic constants, including Vickers hardness, machinability index, elastic anisotropy, and thermodynamic properties and parameters. The structural, elastic, electrical, optical, thermodynamic, and vibrational properties of aluminium hydrides $XAlH_6$ (X = La, Ce, and Pr) have not all been documented in previous investigations. The main aim of the present work is to perform a comprehensive first-principles (DFT) investigation of the structural, mechanical, electronic, optical, and thermodynamic, properties of $XAlH_6$ hydrides (X = La, Ce, and Pr), which have not been previously studied in detail, and to provide a reference database for their potential use in future hydrogen storage and related applications.

2. Method

This study employed density functional theory (DFT) to investigate the structural, electronic, elastic, dynamic, optical, and thermophysical properties of $XAlH_6$ (X = La, Ce, Pr) compounds [18]. The Perdew-Burke-Ernzerhof (PBE) functional under the generalized gradient approximation (GGA) was adopted to model exchange-correlation interactions [19]. Prior to simulations, structural optimizations were conducted using a conjugate-gradient algorithm, ensuring residual atomic forces fell below 0.01 eV/Å, which yielded energy-minimized configurations for subsequent analyses. Norm-conserving Troullier-Martins pseudopotentials [20] were applied to describe core-electron interactions for La, Ce, Pr, Al, and H, while a double-zeta polarized basis set and a 300 Rydberg mesh cutoff ensured precision in electronic structure calculations. The Brillouin zone was sampled via the Monkhorst-Pack scheme [21] with an $8 \times 8 \times 10$ k-point grid to balance computational efficiency and accuracy. Structural parameters, including lattice constants, space group symmetry, and atomic coordinates, were extracted using the KPlot software, which integrates the RGS algorithm for real-time monitoring of structural evolution. Mechanical properties such as bulk modulus, shear modulus, Young's modulus, and Poisson's ratio were derived from second-order elastic constants computed via the stress-strain method within the Siesta framework. The DFT approach, renowned for its reliability in modelling solid-state electronic behaviour, further enabled an assessment of electronic anisotropy using the VELAS [22] program. Thermodynamic properties were evaluated via the Phonopy package [23], leveraging harmonic approximation to predict thermal behaviour. To ensure methodological rigor, convergence tests validated the k-point grid and basis set choices, while the VELAS software provided multidimensional visualization of elastic anisotropy. This comprehensive computational strategy not only elucidated the intrinsic properties of $XAlH_6$ hydrides but also highlighted their potential for energy-related applications, supported by robust theoretical foundations.

3. Results and discussion

3.1. Structural properties

The crystal structure representative of trigonal $XAlH_6$ (X = La, Ce, and Pr) with a space group $R\bar{3}m$ (No. 166) is given in Fig. 1, where the Wyckoff sites for the La/Ce/Pr atoms are at 3b (0, 0, ½), Al at 3a (0, 0, 0),

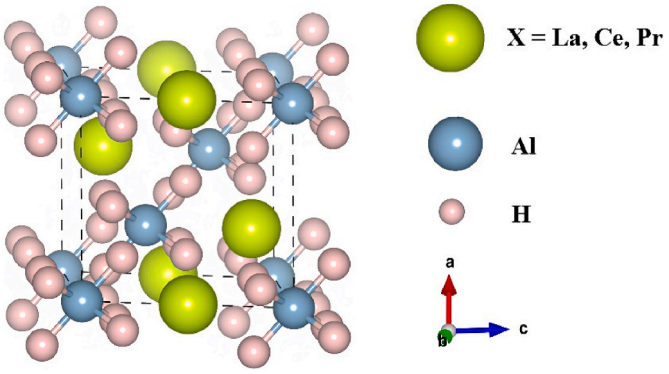

Fig. 1. The crystal structure representatives of $XAlH_6$ (X = La, Ce, and Pr).

and H at 18h (0.4293, 0.2147, 0.5140) respectively, in the unit cell. Table 1 provides the computed lattice constants and material volumes for the materials.

3.2. Stability and hydrogen storage properties

The computed lattice constants of materials along with formation energies are presented in Table 1. Formation energies of materials are computed as follows [24–27];

$$E_{f_{XAlH_6}} = \frac{E_T^{XAlH_6} - [E_X + E_{Al} + 3E_{H_2}]_{bulk}}{24} \quad (1)$$

Where E_T signifies total energy of the system and E_X, E_{Al} and E_H signifies total energies of X, Al and hydrogen in bulk form.

In addition to formation energies, cohesive energies of materials are computed to determine structural stability as follows [25];

$$E_{coh}^{XAlH_6} = \frac{E_T^{XAlH_6} - [E_X + E_{Al} + 3E_{H_2}]_{isolated}}{24} \quad (2)$$

Where E_T signifies total energy of the system and E_X, E_{Al} and E_H signifies total energy of single isolated atom. The synthesisability and thermodynamic stability of all three materials are indicated by their negative formation energies. Stability is indicated by higher positive cohesive energy and higher negative formation energy. Strong atom-to-atom bonds inside a material are indicated by a positive cohesive energy. It can be hypothesized that $PrAlH_6$ is structurally more stable than $CeAlH_6$ and $LaAlH_6$ because $PrAlH_6$ has relatively higher positive cohesive energy (3.98 eV/atom) and a higher negative formation energy per atom (−0.489 eV/atom) than $CeAlH_6$ (4.06 eV/atom, −0.409 eV/atom) and $LaAlH_6$ (3.88 eV/atom, −0.396 eV/atom).

One important factor for these materials is the gravimetric hydrogen density (GHD). This measurement indicates the potential maximum capacity for hydrogen storage within the materials, making it an essential parameter for further investigation of solid-state hydrogen storage materials. The GHD of $XAlH_6$ (X = La, Ce, and Pr) is calculated as detailed below [28,29];

$$C_{wt\%} = \left(\frac{\left(H/M\right) M_H}{M_{Host} + \left(H/M\right) M_H} x\ 100 \right) \% \quad (3)$$

In equation H/M represents the ratio of hydrogen to metal, while M_H refers to the molar mass of hydrogen and M_{Host} indicates the molar weight of the host material. According to the provided equation, the GDH values are calculated to be 3.52 wt % for $LaAlH_6$, 3.50 wt % for $CeAlH_6$, and 3.48 wt % for $PrAlH_6$.

The hydrogen desorption temperature for complex hydrides can be thermodynamically estimated by analysing the interplay between enthalpy and entropy changes during dehydrogenation. Central to this framework is the Gibbs free energy equation, $\Delta G = \Delta H - T\Delta S$, where ΔH denotes the formation enthalpy (computed as E_f), and ΔS represents the total entropy change of the system. Under equilibrium conditions at constant pressure, decomposition occurs when $\Delta G = 0$, yielding the relation $T_{des} = \Delta H/\Delta S$. For practical calculations, the entropy change is approximated as $\Delta S \approx 130.7$ J/mol·K [30], a value dominated by the gaseous H_2 release, as the entropy contribution from the solid-phase reactants is negligible in comparison. This simplification arises from the significant entropy gain associated with hydrogen gas liberation, which outweighs minor solid-state entropy variations during heating. Consequently, the desorption temperature T_{des} serves as a critical metric for evaluating hydride stability, with higher temperatures reflecting stronger thermodynamic retention of hydrogen. The approach underscores the pivotal role of enthalpy optimization in tuning hydride materials for reversible storage applications, while the entropy term remains largely governed by the H_2 phase transition. Such analyses provide foundational insights into the thermal behaviour of complex hydrides, guiding the design of systems with tailored dehydrogenation properties.

The formula is represented as follows,

$$\Delta H = T_d\ x\ \Delta S \quad (4)$$

In this equation, T_d represents the temperature at which hydrogen desorbs. According to this calculation, the hydrogen desorption temperatures are determined to be 292.28 K for $LaAlH_6$, 301.87 K for $CeAlH_6$, and 361.01 K for $PrAlH_6$.

3.3. Single and polycrystalline elastic properties

A material's mechanical characteristics can be used to forecast how it will function in real-world situations and under pressure. A material's utility in various applications can be influenced by its mechanical

Table 2
The calculated elastic constants (GPa) of $XAlH_6$ (X = La, Ce, and Pr).

Materials	Ref.	C_{11}	C_{12}	C_{13}	C_{14}	C_{33}	C_{44}
$LaAlH_6$	This work	141.61	30.15	16.99	−0.04	250.96	28.28
$CeAlH_6$	This work	134.40	20.83	14.59	−1.86	234.34	30.88
$PrAlH_6$	This work	121.43	21.36	17.85	−1.74	232.01	31.60

Table 1
The calculated lattice constants (*a, b,c,* Å), volume (V_0, Å), Formation enthalpy (E_f, eV/atom) and cohesive energy (E_{coh}, eV/atom), gravimetric hydrogen density (GHD, wt.%) and hydrogen desorption temperature (T_d, K) of $XAlH_6$ (X = La, Ce, and Pr).

Materials	Ref.	a	b	c	V_0	E_f (eV/atom)	E_{coh}	GHD	T_d
$LaAlH_6$	This work	6.602	6.602	6.354	239.88	−0.396	3.88	3.52	292.28
	[8]	6.52	6.52	6.29	231.33	−0.434			
$CeAlH_6$	This work	6.453	6.453	6.208	223.92	−0.409	4.06	3.50	301.87
$PrAlH_6$	This work	6.487	6.487	6.134	223.55	−0.489	3.98	3.48	361.01
	[8]	6.47	6.47	6.23	225.53	−0.380			

Table 3
The calculated bulk modulus (B, GPa), shear modulus (G, GPa), B/G ratio, Cauchy Pressure (C_P, GPa), Poisson's ratio (σ), Shear constant (C', GPa), Young's modulus (E, GPa), machinability index (B/C_{44}), and Kleinman parameter (ζ, GPa) of $XAlH_6$ (X = La, Ce, and Pr).

Material	Ref.	B	G	B/G	$C_P(C_{13}\text{-}C_{44})$	σ	C'	E	B/C_{44}	ζ
$LaAlH_6$	This work	71.91	48.26	1.49	−11.28	0.23	55.73	118.32	2.54	0.41
$CeAlH_6$	This work	65.29	49.45	1.32	−16.29	0.20	56.79	118.44	2.11	0.33
$PrAlH_6$	This work	63.07	46.95	1.34	−13.79	0.20	50.04	112.85	1.99	0.36

stability, ductility, brittleness, bonding properties, fracture, hardness, toughness, elastic anisotropy, and other characteristics. The six independent elastic constants for $XAlH_6$ (X = La, Ce, and Pr) are displayed in Table 2, the seventh is $C_{66} = \frac{1}{2}(C_{11} - C_{12})$ and are used to calculate the materials' elastic properties. The polycrystalline elastic moduli are then computed using these values, as shown in Table 3. The Born stability criterion is used to test the mechanical stability of materials [31].

$$C_{11} - C_{12} > 0; (C_{11} + C_{12})C_{33} - 2C_{13}^2 > 0; \ (C_{11} - C_{12})C_{44} - 2C_{14}^2 > 0 \quad (5)$$

$XAlH_6$ (X = La, Ce, and Pr) satisfies equation (5), proving the mechanical stability of these materials.

The bulk modulus (B), a critical indicator of a material's resistance to volumetric deformation under external pressure, reflects its incompressibility, elasticity, and machinability [32]. Comparative analysis reveals a descending trend in volumetric resilience: $LaAlH_6 > CeAlH_6 > PrAlH_6$, suggesting $LaAlH_6$ exhibits the highest dimensional stability. In contrast, the shear modulus (G), which quantifies resistance to shape-preserving shear stresses, demonstrates superior mechanical resilience for $LaAlH_6$ and $CeAlH_6$ relative to $PrAlH_6$, as evidenced by the data in Table 3.

Young's modulus (E), a measure of intrinsic stiffness, correlates with the force required to induce elastic deformation. The hierarchy of rigidity, $CeAlH_6 > LaAlH_6 > PrAlH_6$ (Table 3), positions $CeAlH_6$ as the hardest material within the series, attributed to its maximized E value. This implies $CeAlH_6$ undergoes minimal elastic strain under applied stress, a property critical for applications demanding mechanical robustness. Collectively, these moduli delineate the interplay between volumetric, shear, and tensile responses, offering a framework to tailor hydride materials for specific engineering contexts.

Complementary mechanical analysis incorporating the B/G ratio, Poisson's ratio, and Pugh's ductility criterion [33,34] provides deeper insight into the fracture behaviour of $XAlH_6$ hydrides. Pugh's empirical threshold (B/G = 1.75) distinguishes brittle and ductile responses: values below 1.75 signify brittleness, while higher ratios indicate ductility. As shown in Table 3, all $XAlH_6$ compounds exhibit B/G ratios <1.75, indicating intrinsic brittleness across the series and necessitating careful handling to mitigate fracture risks. Further corroboration arises from the Cauchy pressure ($C_p = C_{13} - C_{44}$), a metric linked to interatomic bonding nature and fracture susceptibility [35]. Negative C_p values, observed for all $XAlH_6$ phases, imply directional bonding (e.g., covalent or angular interactions), which typically engenders brittle failure. In contrast, positive C_p values correlate with metallic bonding and ductile behaviour. The consistently negative C_p values for $LaAlH_6$, $CeAlH_6$, and $PrAlH_6$ thus align with their low B/G ratios, reinforcing the dominance of covalent-like interactions that limit plastic deformation. These combined criteria underscore the inherent brittleness of $XAlH_6$ hydrides, critical for assessing their mechanical reliability in hydrogen storage or structural applications.

Poisson's ratio (σ), a critical parameter for evaluating mechanical behaviour, further elucidates the fracture resistance and bonding nature of $XAlH_6$ (X = La, Ce, Pr) hydrides. As Frantsevich's criterion [36], materials with σ < 0.26 exhibit brittle characteristics, while ductility dominates at higher values. The calculated σ values for all $XAlH_6$ phases (Table 3) fall below this threshold, aligning with their previously identified brittleness. Additionally, σ serves as a probe for interatomic interactions: solids governed by central forces typically exhibit σ between 0.25 and 0.50 [37], whereas non-central interactions, such as directional or covalent bonding, yield ratios outside this range. The sub 0.26 σ values observed here suggest non-central forces dominate in $XAlH_6$, consistent with their angular bonding tendencies. The intermediate σ magnitudes (between metallic (σ ≈ 0.33) and covalent (σ → 1.0) benchmarks [38]) imply a hybrid electronic structure. This semi-metallic character, arising from partial electron delocalization alongside covalent-like directional bonds, may influence electrical conductivity and deformation mechanisms. Such duality underscores the complex interplay between bonding anisotropy and mechanical response in these hydrides, offering avenues for tuning properties through compositional or structural modifications. Collectively, Poisson's ratio analysis reinforces the brittleness of $XAlH_6$ while highlighting their transitional bonding nature, critical for applications requiring balanced electronic and mechanical performance.

The tetragonal shear modulus (C′), defined as $C' = \frac{C_{11}-C_{12}}{2}$, serves as a critical indicator of dynamic stability and mechanical rigidity in crystalline materials [39]. A positive (C′) value confirms structural resilience against shear deformations, whereas a negative value implies susceptibility to dynamic instabilities. As shown in Table 3, the computed (C') values for $XAlH_6$ (X = La, Ce, and Pr) are uniformly positive, confirming the thermodynamic stability of these hydrides under mechanical stress.

The Kleinman parameter (ζ), which quantifies the relative displacement of cationic and anionic sublattices during volume-conserving lattice distortions [40], provides insights into a material's resistance to bond-angle (bending) versus bond-length (stretching) deformations. This dimensionless parameter, calculated via

$$\zeta = \frac{C_{11} + 8C_{12}}{7C_{11} + 2C_{12}} \quad (6)$$

ranges between 0 and 1. A value approaching 0 signifies dominance of bond stretching in resisting external stress, while higher values (closer to 1) emphasize bond bending. For $XAlH_6$ compounds (Table 3), ζ lies marginally below 0.50, suggesting a moderate contribution from bond bending and a comparatively stronger influence of bond stretching in maintaining mechanical integrity. This sub-unity behavior highlights the interplay between these deformation modes, with axial rigidity playing a slightly more pronounced role in stabilizing the lattice. These findings align with the positive C′ values, collectively affirming the robust mechanical and dynamic stability of the studied aluminohydrides.

The machinability index, quantified by the ratio B/C_{44}, provides critical insights into a material's ease of processing, where a lower C_{44} shear modulus correlates with enhanced machinability a hallmark of ductile or softer systems [41]. Conversely, materials with elevated hardness typically exhibit diminished machinability indices due to their

Table 4
The computed hardnesses of $XAlH_6$ (X = La, Ce, and Pr).

Material	Ref.	H_v (Chen)	$H_{v\ (Tian)}$	H_v (Teter)	H_v (Miao)	H_v (Mazhnik)
$LaAlH_6$	This work	9.12	8.48	7.29	8.82	5.52
$CeAlH_6$	This work	11.15	10.11	7.47	9.97	6.38
$PrAlH_6$	This work	10.46	9.53	7.09	9.33	5.91

inherent resistance to deformation. For $XAlH_6$ (X = La, Ce, and Pr), hardness values were computed using five empirical models: Chen's [42], Tian's [43], Miao's [44], Teter's [45], and Mazhnik's [46] (Eqs. (7)–(11)), with results consolidated in Table 4. Notably, materials are classified as "hard" if their Vickers hardness exceeds 10 GPa and "superhard" beyond 40 GPa [32]. The calculated hardness values for $XAlH_6$ compounds fall below the 10 GPa threshold, precluding their classification as hard materials. As evidenced by Table 3, $LaAlH_6$ exhibits the highest machinability index and the lowest hardness within the series, underscoring its comparatively softer mechanical profile relative to $CeAlH_6$ and $PrAlH_6$. This inverse relationship between hardness and machinability aligns with theoretical expectations, suggesting that $LaAlH_6$'s reduced resistance to shear (C_{44}) facilitates easier mechanical processing. Such trends highlight the interplay between intrinsic mechanical properties and practical manufacturability, positioning $LaAlH_6$ as the most pliant candidate among the studied aluminohydrides for applications requiring deformability.

$$H_v^{Chen} = 2\,x\left[\left(\frac{G}{B}\right)^2 x\,G\right]^{0.585} - 3 \tag{7}$$

$$H_V^{Tian} = 0.92\,x\left(\frac{G}{B}\right)^{1.137} G^{0.708} \tag{8}$$

$$H_v^{Teter} = 0.151\,x\,G \tag{9}$$

$$H_V^{Miao} = \frac{(1-2\sigma)\,x\,E}{6\,x\,(1+\sigma)} \tag{10}$$

$$H_V^{Mazhnik} = Y_o\chi(\sigma)E \tag{11}$$

In equation (11), the variable $\chi(\sigma)$ is influenced by Poisson's ratio and can be represented as [47];

$$\chi(\sigma) = \frac{1 - 8.5\sigma + 19.5\sigma^2}{1 - 7.5\sigma - 12.2\sigma^2 + 19.6\sigma^3} \tag{12}$$

The value of Y_o is 0.096, and it has no dimensions.

3.4. Elastic anisotropy

Elastic anisotropy, an inherent property governed by directional variations in elastic constants, profoundly influences the micromechanical behaviour and macroscopic performance of crystalline materials. To quantify this directional dependence, anisotropy indices are employed, with values deviating from unity signalling pronounced anisotropy. For isotropic systems, these indices equal one, while anisotropic materials exhibit deviations reflective of structural asymmetry [42]. In this study, the elastic anisotropy of $XAlH_6$ (X = La, Ce, and Pr) is systematically evaluated through multiple metrics: the Zener anisotropy factor (A), shear anisotropy parameters (A_1, A_2, A_3), compressibility anisotropy (A_B), shear anisotropy percentage (A_G), and the universal anisotropy index (A^U) [48]. These parameters, computed using established formulae and tabulated in Table 5, provide a comprehensive assessment of directional mechanical disparities. The Zener factor (A), for instance, quantifies deviations from cubic symmetry in shear response, while A^U offers a holistic measure of elastic anisotropy. By analysing these indices, the study elucidates how crystallographic directionality governs deformation resistance and mechanical integrity in $XAlH_6$ hydrides, offering insights critical for applications requiring tailored anisotropic properties.

$$A = \frac{2\,C_{44}}{C_{11} - C_{12}} \tag{13}$$

$$A_1 = \frac{4\,C_{44}}{C_{11} + C_{33} - 2C_{13}} \tag{14}$$

$$A_2 = \frac{4\,C_{55}}{C_{22} + C_{33} - 2C_{23}} \tag{15}$$

$$A_3 = \frac{4\,C_{66}}{C_{11} + C_{22} - 2C_{12}} \tag{16}$$

The shear anisotropy factors A_1, A_2 and A_3 quantify directional disparities in elastic response across distinct crystallographic planes. Specifically, A_1 characterizes anisotropy in the [010]-[011] plane, while A_2 and A_3 describe deviations in the [010] and [001] planes, respectively [49]. These parameters reflect how shear stiffness varies with crystallographic orientation, with the Zener factor serving as a consolidated metric for overall elastic anisotropy. As summarized in Table 5, $A_3 = 1$ for all $XAlH_6$ (X = La, Ce, Pr) compounds, indicating isotropic behaviour in the [001] plane. However, deviations in A_1 and A_2 from unity reveal pronounced anisotropy in other planes. Among the studied hydrides, $LaAlH_6$ exhibits the most marked anisotropy, whereas $PrAlH_6$ shows the weakest directional dependence, suggesting a gradation in structural symmetry across the series.

Further insights into polycrystalline anisotropy are provided by the compressibility (A_B) and shear (A_G) anisotropy indices, as defined by Chung and Buessem [50]. These metrics evaluate the degree to which bulk and shear moduli deviate from isotropic averages, offering a macroscopic perspective on directional mechanical behaviour. The interplay between these anisotropy indices and the shear factors underscores the complex relationship between crystallographic symmetry and mechanical performance in $XAlH_6$ systems, with implications for their application in environments requiring tailored anisotropic responses.

$$A_B = \frac{B_V - B_R}{B_V + B_R} \tag{17}$$

$$A_G = \frac{G_V - G_R}{G_V + G_R} \tag{18}$$

The elastic anisotropy of polycrystalline systems is conventionally assessed through the Voigt and Reuss approximations, which define upper (Voigt: B_V, G_V) and lower (Reuss: B_R, G_R) bounds for the bulk modulus and shear modulus, respectively. These bounds underpin the calculation of dimensionless anisotropy indices A_B (compressibility) and A_G (shear), where values approaching 0 signify isotropic behaviour and deviations toward 1 reflect increasing directional dependence. For $XAlH_6$ (X = La, Ce, Pr), the computed A_B indices approach zero (Table 5), indicating minimal directional variation in compressibility a hallmark of near-isotropic volumetric response under hydrostatic stress. In contrast, A_G retains non-negligible values across all compounds, revealing persistent anisotropy in shear deformation. This dichotomy suggests that while these hydrides resist volume changes uniformly across crystallographic directions, their shear rigidity remains sensitive

Table 5
The computed anisotropy factor (A), shear anisotropic factors (A_1, A_2, and A_3 on the (100), (010) and (001) planes), percentage of anisotropy (A_B, A_G) and the universal elastic anisotropy index (A^u) of $XAlH_6$ (X = La, Ce, and Pr).

Material	*Ref.*	*A*	A_1	A_2	A_3	A_B	A_G	A^U
$LaAlH_6$	This work	0.507	0.315	0.315	1.000	0.024	0.115	1.342
$CeAlH_6$	This work	0.544	0.364	0.364	1.000	0.026	0.090	1.049
$PrAlH_6$	This work	0.632	0.398	0.398	1.000	0.038	0.076	0.901

to lattice orientation. Such behaviour aligns with the earlier observation of shear anisotropy factors (A_1, A_2) deviating from unity, reinforcing the interplay between directional bonding and mechanical anisotropy in these systems.

The universal anisotropy index (A^U), defined as

$$A^U = 5\frac{G_V}{G_R} + \frac{B_V}{B_R} - 6 \tag{19}$$

quantifies the elastic anisotropy of single crystals, where deviations from zero directly correlate with the degree of directional mechanical disparity [50]. For isotropic systems, $A^U = 0$, while non-zero values signal increasing anisotropy. As calculated for $XAlH_6$ (X = La, Ce, Pr), A^U follows the trend $LaAlH_6 > CeAlH_6 > PrAlH_6$, confirming $LaAlH_6$ as the most anisotropic and $PrAlH_6$ as the least within the series (Table 5). This hierarchy aligns with earlier observations of shear anisotropy factors (A_1, A_2) deviating from unity, underscoring the role of lattice symmetry in governing mechanical behaviour.

To visualize anisotropy, three-dimensional contour plots of Young's modulus, shear modulus, and Poisson's ratio were generated via the VELAS software [22] (Fig. 2). Isotropic materials produce spherical profiles, whereas anisotropic systems exhibit distorted geometries. The plots reveal subtle but discernible deviations from sphericity across all compounds, consistent with the fractional anisotropy indices in Table 5. Notably, LaAlH6 displays the most pronounced distortion in shear modulus contours, reflecting its elevated A^U value and reinforcing the dominance of (G_V/G_R) in driving anisotropy.

These results collectively confirm that all $XAlH_6$ hydrides exhibit measurable elastic anisotropy, as evidenced by non-unitary shear

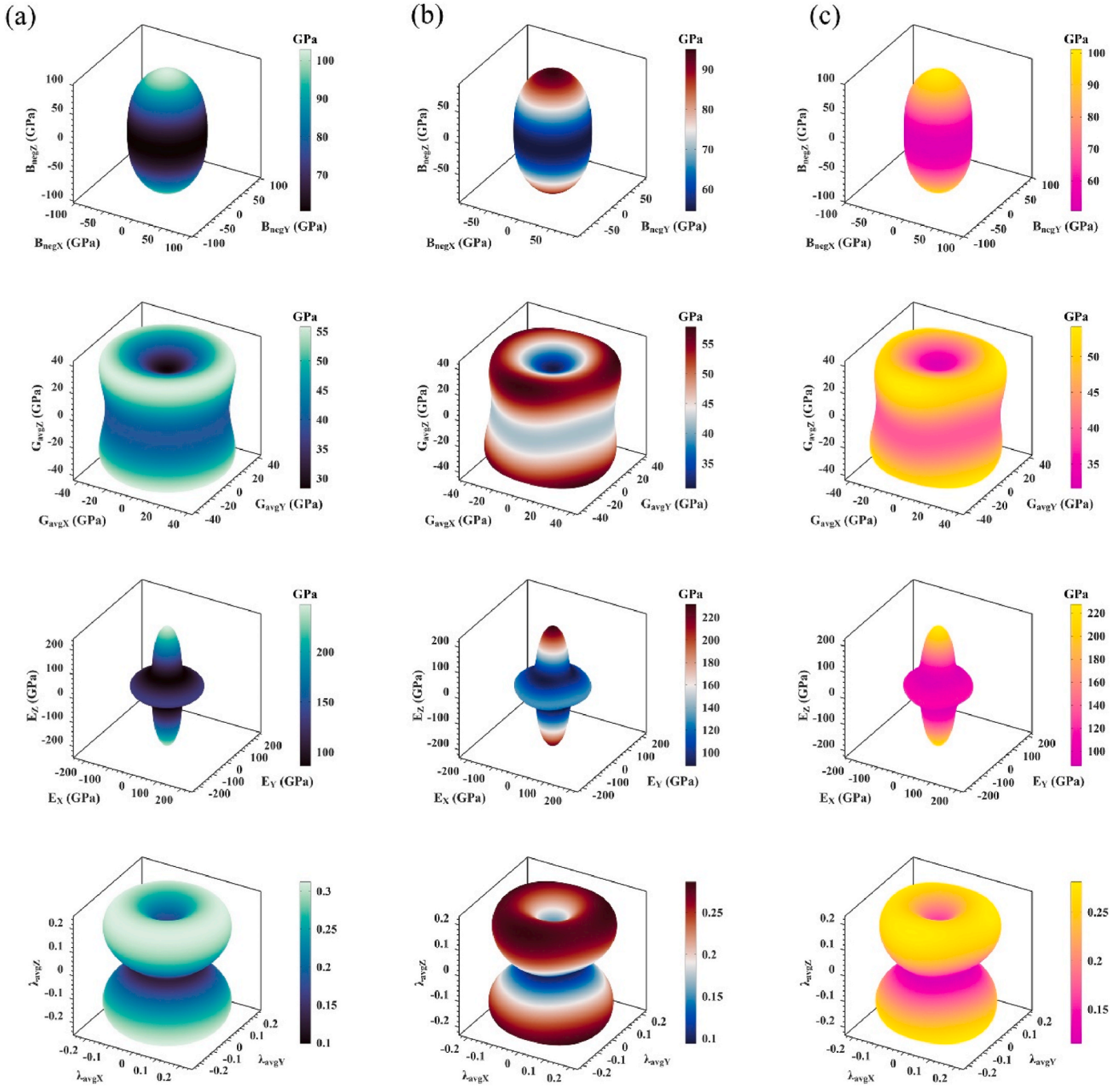

Fig. 2. 3D curves of Bulk modulus, Young's modulus, Shear modulus, and Poisson's ratios of $XAlH_6$ (X = La, Ce, and Pr).

anisotropy factors ($A_1 \neq 1$, $A_2 \neq 1$) and non-zero A^U values. The gradation in anisotropy across the series greatest in $LaAlH_6$ and diminishing in $PrAlH_6$ highlights the interplay between cationic substitution (La → Pr) and lattice symmetry, offering insights into how compositional tuning can modulate anisotropic responses in complex hydrides.

3.5. Thermo-elastic properties

To evaluate the thermal behaviour of $XAlH_6$ (X = La, Ce, and Pr), key thermodynamic parameters including the Debye temperature (Θ_D) were systematically analysed (Table 6). These properties are intrinsically interdependent, with Θ_D derived from elastic moduli via acoustic velocity calculations. The transverse (v_t) and longitudinal (v_l) sound velocities were computed as [51,52]:

$$V_t = \sqrt{\frac{G}{\rho}} \tag{20}$$

$$V_l = \sqrt{\frac{3B + 4G}{3\rho}} \tag{21}$$

where G, B, and ρ denote shear modulus, bulk modulus, and density, respectively. The mean acoustic velocity (v_m) was determined using:

$$V_m = \left[\frac{1}{3}\left(\frac{1}{V_l^3} + \frac{1}{V_t^3}\right)\right]^{-\frac{1}{3}} \tag{22}$$

enabling Θ_D to be expressed as [51,52]:

$$\Theta_D = \frac{h}{k_B}\left[\frac{3n}{4\pi}\left(\frac{N_{A\rho}}{M}\right)\right]^{\frac{1}{3}} V_m \tag{23}$$

Here, h, k_B, N_A, n, and M represent Planck's constant, Boltzmann's constant, Avogadro's number, atoms per formula unit, and molar mass, respectively.

The Debye temperature serves as a critical indicator of bond strength and lattice rigidity, inversely correlating with molecular weight. Elevated θ_D values signify robust chemical bonding and enhanced thermal stability, influencing properties such as heat capacity and thermal conductivity [53]. Among the studied hydrides, θ_D follows the trend $LaAlH_6 > CeAlH_6 > PrAlH_6$, reflecting diminishing bond strength with increasing atomic mass (La → Pr). This trend aligns with the inverse relationship between θ_D and molar mass, as heavier atoms reduce vibrational frequencies. Notably, sound velocities (V_t, V_l) correlate with bulk modulus and density: higher velocities correspond to stiffer lattices (larger B) and lower densities. As shown in Table 6, $LaAlH_6$ exhibits the highest V_t and V_l, consistent with its superior bulk modulus and reduced density relative to $CeAlH_6$ and $PrAlH_6$. These findings underscore the interplay between elastic properties, atomic mass, and thermal characteristics, providing a framework for tailoring hydrides for applications requiring specific thermal and mechanical responses.

The thermal stability and lattice dynamics of $XAlH_6$ (X = La, Ce, and Pr) were further investigated through melting temperature (T_m), Grüneisen parameter (γ), and minimum thermal conductivity (K_{min}) analyses. For trigonal systems, T_m was estimated via the empirical relation:

$$T_m = 354 + 1.5(2C_{11} + C_{33}) \pm 300K \tag{24}$$

where C_{11} and C_{33} are elastic constants [54]. All compounds exhibit $T_m > 1000$ K, confirming their suitability for high-temperature applications due to robust atomic bonding and structural integrity.

The Grüneisen parameter calculated as

$$\gamma = \frac{3}{2}\left(\frac{1+\sigma}{2-3\sigma}\right) \tag{25}$$

where σ is Poisson's ratio, quantifies lattice anharmonicity and phonon scattering efficiency [55]. Values of γ for $XAlH_6$ fall within the polycrystalline benchmark range of 0.85–3.53 [56], correlating with Poisson ratios σ between 0.05 and 0.46. $LaAlH_6$ exhibits the highest γ (indicating pronounced phonon anharmonicity and suppressed thermal conductivity), while $CeAlH_6$ shows the lowest γ, suggesting stronger harmonic lattice vibrations and enhanced heat transport.

To assess high-temperature thermal performance, minimum thermal conductivity (K_{min}) was computed via Clarke's model [52,57,58]:

$$\kappa_{min}^{Clarke} = 0.87 x k_B \left(\frac{M}{n\rho N_A}\right)^{-\frac{2}{3}} \left(\frac{E}{\rho}\right)^{\frac{1}{2}} \tag{26}$$

where k_B, M, n, ρ, N_A, and E denote Boltzmann's constant, molar mass, atoms per formula unit, density, Avogadro's number, and Young's modulus, respectively. The calculated K_{min} follows $CeAlH_6 > LaAlH_6 > PrAlH_6$, consistent with their γ trends. While these values represent idealized lower bounds for defect-free crystals, practical thermal conductivity is reduced by phonon scattering at defects, grain boundaries, and lattice imperfections effects amplified at elevated temperatures.

These results underscore the inverse relationship between anharmonicity (γ) and thermal conductivity, highlighting $CeAlH_6$ as the most thermally conductive candidate. The interplay of bonding strength, lattice dynamics, and defect-mediated scattering provides critical insights for tailoring $XAlH_6$ hydrides in high-temperature environments where thermal management is paramount.

3.6. Electronic properties

The electronic band structures and partial density of states (PDOS) of $XAlH_6$ (X = La, Ce, and Pr) were computed to elucidate their electronic properties, as illustrated in Fig. 3. The Fermi level (E_F), marked at 0 eV (dashed line), delineates valence bands (below E_F) and conduction bands (above E_F). Materials are classified as metallic if bands intersect E_F, whereas semiconducting or insulating behavior arises when a bandgap separates the valence and conduction bands. Semiconductors are further categorized as direct (valence band maximum and conduction band minimum share the same symmetry point) or indirect (these extrema occur at distinct symmetry points). For $LaAlH_6$ and $PrAlH_6$, bandgaps of 2.05 eV and 0.95 eV, respectively, are observed between the valence band maximum and conduction band minimum near E_F (Fig. 4), confirming their semiconducting nature. In contrast, $CeAlH_6$ exhibits metallic behavior due to band crossings at E_F. Complementary PDOS analyses reveal orbital-specific contributions to these electronic states. In $LaAlH_6$, the valence band is dominated by H-1s orbitals, while the conduction band is primarily shaped by La-5d states. For $CeAlH_6$, H-1s orbitals similarly govern the valence region, but the conduction band shows a dual contribution: Ce-5d states dominate between 0 and 2 eV, while La-5d states extend up to 6 eV. $PrAlH_6$ follows an analogous trend,

Table 6
The calculated density (ρ, g/cm^3), acoustic velocities (V_t, V_l, V_m, m/s), melting temperature (T_m, K), Debye temperature (Θ, K), Grüneisen parameter (γ) and minimum thermal conductivity (κ, W.K^{-1}.m^{-1}) of $XAlH_6$ (X = La, Ce, and Pr).

Material	Ref.	ρ	V_t	V_l	V_m	T_m	Θ	γ	κ
$LaAlH_6$	This work	3.69	3167.69	6078.71	4005.18	1155.29	559.48	1.39	1.22
$CeAlH_6$	This work	3.85	3582.69	5836.44	3954.25	1108.72	559.15	1.28	1.23
$PrAlH_6$	This work	3.88	3480.31	5693.96	3842.94	1066.32	543.70	1.29	1.20

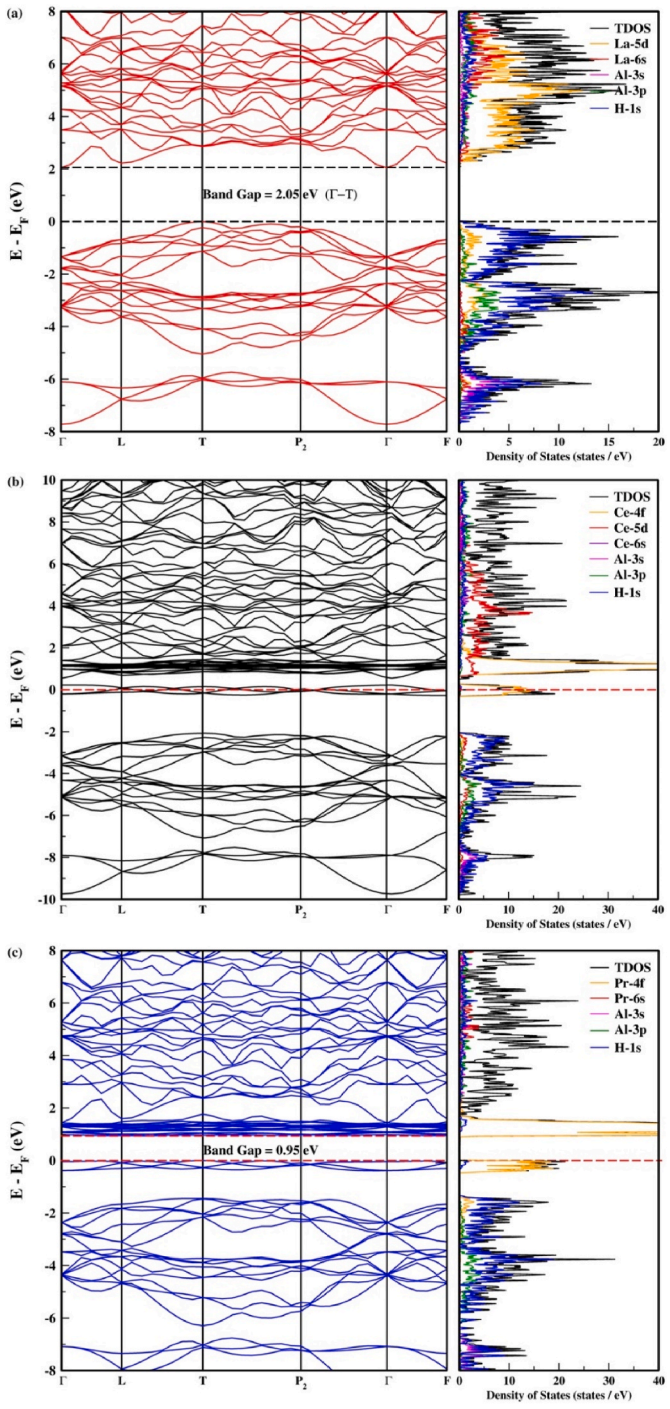

Fig. 3. Electronic band structures of $XAlH_6$ (X = La, Ce, and Pr).

with H-1s orbitals defining the valence band and Pr-4f states contributing significantly to the low-energy conduction region (0–2 eV). These findings highlight the pivotal role of hydrogen's 1s electrons in valence band formation across all compounds, while the conduction characteristics are dictated by the distinct d- or f-orbital hybridization of the rare-earth cations (La, Ce, and Pr). The semiconducting behavior of $LaAlH_6$ and $PrAlH_6$, coupled with $CeAlH_6$'s metallicity, underscores the tunability of electronic properties through cationic substitution in this hydride series. Such insights are critical for applications in optoelectronics and energy conversion, where bandgap engineering and charge transport mechanisms are paramount.

3.7. Optical properties

Understanding optical characteristics is crucial for analysing how a material reacts to incoming electromagnetic waves. They are also crucial for investigating potential optoelectronic and photovoltaic device uses. It is crucial to consider the reactions to the infrared, visible, and ultraviolet spectrum for optoelectronic and photovoltaic device uses. All the various energy dependent optical constants, namely the real and imaginary parts of the dielectric constants, $\varepsilon_1(\omega)$ and $\varepsilon_2(\omega)$, respectively, the real part of the refractive index $n(\omega)$, the optical conductivity $\sigma(\omega)$, the absorption coefficient $\alpha(\omega)$, the reflectivity $R(\omega)$, and the loss function $L(\omega)$ are responsible for determining this response with respect to the incident electromagnetic wave. Optical properties are typically determined by analysing the complex dielectric function. The real part of the dielectric function (ε_1) is obtained through the Kramers-Kronig relations, while the imaginary part (ε_2) is calculated by examining the momentum matrix elements between occupied and unoccupied electronic states. The dielectric function $\varepsilon(\omega)$ consists of two components: the real part, $\varepsilon_1(\omega)$, and the imaginary part, $\varepsilon_2(\omega)$, expressed as $\varepsilon(\omega) = \varepsilon_1(\omega) + i\,\varepsilon_2(\omega)$. Fig. 4(a–c) shows the calculated real portion of the dielectric function $\varepsilon_1(\omega)$ and the imaginary part $\varepsilon_2(\omega)$ within the incident photon energy range up to 30 eV for all materials. The real part $\varepsilon_1(\omega)$ causes energy dissipation and damping in the wave, while the imaginary part $\varepsilon_2(\omega)$ is linked to the material's polarization and energy storage capabilities. Fig. 4(a–c) shows the calculated static dielectric function $\varepsilon_1(0)$ for each material, with values of 6.56 for $LaAlH_6$, 7.90 for $CeAlH_6$, and 7.20 for $PrAlH_6$. The value of $CeAlH_6$ is larger than both $PrAlH_6$ and $LaAlH_6$, which means that $CeAlH_6$ dissipates more energy than other materials. The imaginary part of the dielectric functions of the compound $CeAlH_6$ start at 0 eV, indicating their metallic nature. $LaAlH_6$ and $PrAlH_6$, however, does not start at 0 eV, supporting the semiconductor nature of them. All calculated materials show a gradual increase from 2 to 5 eV. The imaginary part of the dielectric function for $LaAlH_6$, $CeAlH_6$ and $PrAlH_6$ reaches its maximum at 4.10, 4.43 and 4.59 eV, respectively. Overall, the analysis of the dielectric function indicates that both materials are responsive to low photon energy levels.

Fig. 4 (d) shows the analysed refractive index $n(\omega)$. The static refractive index n (0) values for $LaAlH_6$, $CeAlH_6$, and $PrAlH_6$ are 2.56, 2.81, and 2.73, respectively, based on their refractive index spectrum. $LaAlH_6$, $CeAlH_6$, and $PrAlH_6$ have maximal peak refractive index of 3.42, 3.48, and 2.98, respectively, at 3.36, 3.09, and 2.70 eV photon energy. The refractive index is a crucial parameter for determining the extent of light bending, particularly in photoelectric uses. Photons decelerate upon entering a substance due to interactions with electrons, resulting in a refractive index greater than 1. Materials with higher refractive index, have increased photon delay when light passes through them. Enhancing the electrical densities of a material also increases the refractive index value.

Optical absorption properties play a vital role in influencing the performance of devices used in optoelectronics and photovoltaic materials, since they are responsible for the generation and transmission of charge carriers through the absorption of light. The absorption curves for the three different materials are presented in Fig. 3 (e). Absorption starts at 2.05 and 0.95 eV for $LaAlH_6$ and $PrAlH_6$, respectively, which agree well with the band gap values of both compounds. For the $CeAlH_6$, absorption starts at 0 eV. For the three materials studied, the absorption increases by 10 eV, decreases from 10 eV to 18 eV and then reaches maximum values at 21.65, 22.35 and 23.43 eV for $LaAlH_6$, $CeAlH_5$ and $PrAlH_6$, respectively. These findings show that $XAlH_6$ (La, Ce, and Pr) is very good at absorbing vacuum far ultraviolet light, which suggests that it could be a useful material for optoelectronic devices.

Fig. 3 (f) displays the optical reflectivity calculated from the dielectric function across an energy range from 0 eV to 40 eV. The zero-frequency reflectivity R (0) of $LaAlH_6$, $CeAlH_6$ and $PrAlH_6$ is 0.19, 0.22 and 0.21 respectively. Up to 10 eV the reflectivity increases slightly, after 10 eV it drops to about 18 eV. It then reaches a maximum at 23.22

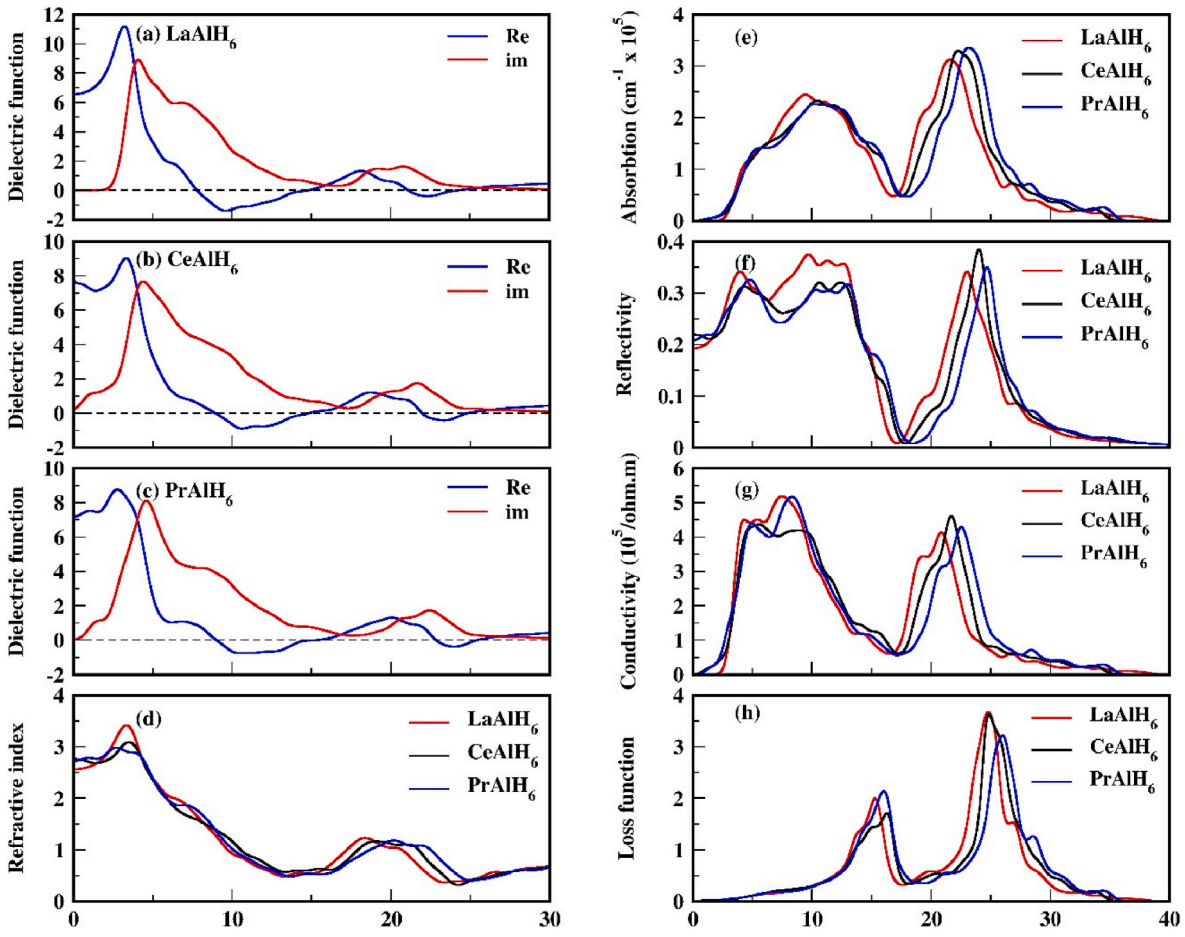

Fig. 4. Optical properties of $XAlH_6$ (X = La, Ce, and Pr).

(33 %), 24.20 (38 %) and 25.02 eV (34 %) for $LaAlH_6$, $CeAlH_6$ and $PrAlH_6$ respectively. In the visible spectrum, electromagnetic radiation with a polarization of [1 0 0] has a reflectivity of less than 40 %. Therefore, $XAlH_6$ can be utilized as an anti-reflection material for this specific polarization.

The optical conductivity, denoted by the symbol σ(ω), is a term that specifically describes the manner in which an electromagnetic field induces electrons to conduct. Fig. 3 (g) illustrates the σ(ω) value that was determined by utilizing the dielectric function. The optical conductivity, as in absorption, starts at 0 for $CeAlH_6$ and $PrAlH_6$, while $LaAlH_6$ starts at 2.05 eV, which confirms the metallic nature of $CeAlH_6$ and $PrAlH_6$ and the semiconducting nature of $LaAlH_6$ obtained from both the band structure and TDOS curves. The optical conductivity increases sharply in the range from 2 to 8 eV. It decreases in the range between 8eV and 17 eV, then increases up to 22 eV, then starts to decrease again and becomes zero at about 35 eV. The maximum values for $LaAlH_6$, $CeAlH_6$ and $PrAlH_6$ are 5.15 x 10^5 $\Omega^{-1}m^{-1}$ at 7.65 eV, 4.58 x 10^5 $\Omega^{-1}m^{-1}$ at 21.75 eV and 5.13 x 10^5 $\Omega^{-1}m^{-1}$ at 8.55 eV, respectively.

Fig. 3 (h) displays the energy loss spectra. The loss energy spectrum has been calculated from equation below using the real and imaginary part of the dielectric constant.

$$L(\omega) = \frac{\varepsilon_2(\omega)}{\varepsilon_1{}^2(\omega) + \varepsilon_2{}^2(\omega)} \tag{27}$$

The loss function is a crucial optical metric utilized to analyse the filtered optical excitation spectra. The energy loss spectrum peak corresponds to a specific incident light energy that provides information about the bulk plasma frequency. Plasma peaks of 25, 25 and 26 eV are obtained for $LaAlH_6$, $CeAlH_6$ and $PrAlH_6$ respectively. In instances where the incident light frequency surpasses the plasma frequency, the material transforms into a transparent state and manifests optical characteristics like those of an insulator. $\varepsilon_2(\omega)$ approaches zero above plasma energy, indicating that the electromagnetic energy lost during transmission through the material is negligible.

4. Conclusions

In this study, first-principles density functional theory calculations were used to comprehensively investigate the structural, mechanical, electronic, thermodynamic, and optical properties of rare earth aluminium hydrides $XAlH_6$ (X = La,Ce, and Pr). The calculated negative formation enthalpies confirm the thermodynamic stability and synthesizability of all three materials, while the Born mechanical stability criteria and positive cohesive energies indicate strong atom-atom bonding. The gravimetric hydrogen densities ranging from 3.48 to 3.52 wt% and hydrogen desorption temperatures between 292 K and 361 K suggest that these hydrides are promising candidates for solid-state hydrogen storage with tuneable release properties depending on the cation species.

Analysis of mechanical properties reveals that all $XAlH_6$ compounds are intrinsically brittle (B/G < 1.75, Poisson's ratio <0.26) with directional bonding but exhibit sufficient bulk and shear moduli to maintain structural integrity under practical conditions. Elastic anisotropy studies highlight that $LaAlH_6$ is the most anisotropic, while $PrAlH_6$ is the most isotropic; this has significant implications for stress distribution during the hydrogen cycle. Thermodynamic parameters, including Debye temperature and minimum thermal conductivity, show a correlation between bond strength, lattice dynamics, and thermal transport, with

$CeAlH_6$ emerging as the most thermally conductive composition.

Electronic structure and optical analyses reveal that $LaAlH_6$ and $PrAlH_6$ are indirect semiconductors with band gaps of 2.05 eV and 0.95 eV, respectively, while $CeAlH_6$ exhibits metallic conductivity. The optical property evaluation confirms good absorption in the far-ultraviolet region and low reflectance in the visible region, indicating potential for optoelectronic and anti-reflective applications. Overall, this work enriches the database of rare earth aluminium hydrides and establishes a detailed property framework that can guide the rational design of a new generation of hydrogen storage materials with optimized thermodynamic, mechanical, and electronic properties.

CRediT authorship contribution statement

Çağatay Yamçıçıer: Writing – review & editing, Writing – original draft, Visualization, Supervision, Software, Resources, Methodology, Investigation, Formal analysis, Data curation, Conceptualization. **Selgin Al:** Writing – review & editing, Writing – original draft, Resources, Methodology, Formal analysis. **Cihan Kürkçü:** Writing – review & editing, Writing – original draft, Resources, Methodology, Investigation, Formal analysis, Conceptualization.

Novelty

This study presents the first comprehensive theoretical investigation of trigonal $XAlH_6$ (X = La, Ce, Pr) aluminohydrides, a novel class of materials unexplored in prior experimental orcomputational research. Employing density functional theory, we systematically elucidate theirstructural, mechanical, electronic, thermodynamic, optical, and hydrogen storage properties.The findings reveal mechanical and thermodynamic stability, brittle mechanical behavior, anddistinct electronic characteristics, with $LaAlH_6$ and $PrAlH_6$ exhibiting semiconductingbandgaps of 2.05 eV and 0.95 eV, respectively, and CeAlH6 displaying metallic conductivity. With gravimetric hydrogen densities of 3.48–3.52 wt% and low reflectivity (<40 %) in thevisible spectrum, $XAlH_6$ compounds emerge as promising candidates for solid-state hydrogenstorage and optoelectronic applications. This work not only introduces a new family ofaluminohydrides but also provides a robust computational framework for tailoring theirproperties for energy storage and advanced technological applications.

Declaration of competing interest

The authors declare that they have no known competing financial interests or personal relationships that could have appeared to influence the work reported in this paper.

Acknowledgment

This study was supported by the Kırşehir Ahi Evran University under Scientific Research Project No: TBY.A1.24.001.

Data availability

Data will be made available on request.

References

[1] M. Umer, et al., First principles investigation of structural, mechanical, thermodynamic, and electronic properties of Al-based perovskites $XAlH_3$ (X=K, Rb, Cs) for hydrogen storage, Int. J. Hydrogen Energy 61 (2024) 820–830.
[2] C. Kurkcu, S. Al, C. Yamcicier, Investigation of mechanical properties of $KCaH_3$ and $KSrH_3$ orthorhombic perovskite hydrides under high pressure for hydrogen storage applications, Eur. Phys. J. B 95 (11) (2022) 180.
[3] S. Al, Mechanical and electronic properties of perovskite hydrides $LiCaH_3$ and $NaCaH_3$ for hydrogen storage applications, Eur. Phys. J. B 94 (9) (2021) 182.
[4] S. Li, X. Ju, C. Wan, *Pressure-induced phase transitions in $LiBH_4$: density functional theory calculations*, Int. J. Hydrogen Energy 39 (17) (2014) 9330–9338.
[5] C. Li, et al., Research progress in $LiBH_4$ for hydrogen storage: a review, Int. J. Hydrogen Energy 36 (22) (2011) 14512–14526.
[6] P. Vajeeston, et al., *Structural stability of alkali boron tetrahydrides ABH_4 (A = Li, Na, K, Rb, Cs) from first principle calculation*, J. Alloys Compd. 387 (1) (2005) 97–104.
[7] A. Züttel, et al., *Hydrogen storage properties of $LiBH_4$*, J. Alloys Compd. 356–357 (2003) 515–520.
[8] C. Weidenthaler, et al., Complex rare-earth aluminum hydrides: mechanochemical preparation, crystal structure and potential for hydrogen storage, J. Am. Chem. Soc. 131 (46) (2009) 16735–16743.
[9] T. Sato, et al., *Crystal structural determination of $SrAlD_5$ with corner-sharing AlD_6 octahedron chains by X-ray and Neutron diffraction* 8 (2) (2018) 89.
[10] W. Khan, The first principles insights of aluminum-based hydrides for hydrogen storage application, Int. J. Hydrogen Energy 63 (2024) 596–608.
[11] X. Fan, et al., *Preparations and de/re-hydrogenation properties of $Li_xNa_{3-x}AlH_6$ (x=0.9–1.3) non-stoichiometric compounds*, J. Alloys Compd. 729 (2017) 648–654.
[12] F. Yang, Y. Pan, I.P. Jain, Single atom enhanced the catalytic activity of borophene catalysts for hydrogen evolution reaction, Int. J. Hydrogen Energy 140 (2025) 223–232.
[13] Y. Pan, J. Gao, *Exploring the hydrogen storage capacity, dehydrogenated mechanism, electronic and optical properties of $AMMgH_3$ hydrides for hydrogen storage*, J. Energy Storage 124 (2025) 116869.
[14] J. Gao, et al., *Exploring the structure, hydrogen storage capacity and hydrogen storage mechanism of $X_3N_3H_6$ hydrides for hydrogen storage*, Appl. Mater. Today 44 (2025) 102755.
[15] Y. Zhu, et al., *Investigation of structure, dehydrogenated behavior, mechanical and physical properties of $LiAlH_4$ hydrogen storage material*, Int. J. Hydrogen Energy 136 (2025) 11–20.
[16] Y. Pan, Y. Zhu, *Theoretical prediction of novel phase, phonon dynamics and physical properties of $KAlH_4$ hydride for hydrogen storage*, Int. J. Hydrogen Energy 131 (2025) 221–228.
[17] Y. Pan, J. Gao, *Transition metal improved the dehydrogenated capacity, electronic and optical properties of the layered V_2C MXene for hydrogen evolution reaction*, Surf. Interfaces 62 (2025) 106185.
[18] P. Ordejón, E. Artacho, J.M. Soler, Self-consistent order-N density-functional calculations for very large systems, Phys. Rev. B 53 (16) (1996) R10441.
[19] J.P. Perdew, K. Burke, M. Ernzerhof, Generalized gradient approximation made simple, Phys. Rev. Lett. 77 (18) (1996) 3865.
[20] N. Troullier, J.L. Martins, Efficient pseudopotentials for plane-wave calculations, Physical review B 43 (3) (1991) 1993.
[21] H.J. Monkhorst, J.D. Pack, Special points for Brillouin-zone integrations, Physical review B 13 (12) (1976) 5188.
[22] Z. Ran, et al., VELAS: an open-source toolbox for visualization and analysis of elastic anisotropy, Comput. Phys. Commun. (2022) 108540.
[23] A. Togo, First-principles phonon calculations with phonopy and Phono3py, J. Phys. Soc. Jpn. 92 (1) (2022) 012001.
[24] M.I. Hussain, et al., *Probing the structural, electronic, mechanical strength and optical properties of tantalum-based oxide perovskites $ATaO_3$ (A = Rb, Fr) for optoelectronic applications: First-principles investigations*, Optik 219 (2020) 165027.
[25] M.I. Hussain, R.M.A. Khalil, *Density functional theory studies of the structural, optoelectronic, bond stiffness and lattice dynamical properties of double perovskite oxides M_2YVO_6 (M= Mg, Sr): promising candidates for optoelectronic applications*, Mater. Sci. Semicond. Process. 152 (2022) 107050.
[26] M.I. Hussain, R.M.A. Khalil, F. Hussain, *Computational exploration of structural, electronic, and optical properties of novel combinations of inorganic ruddlesden–popper layered perovskites Bi_2XO_4 (X = Be, mg) using tran and blaha-modified Becke–Johnson approach for optoelectronic applications* 9 (5) (2021) 2001026.
[27] O. Örnek, et al., *Electronic and elastic properties cubic of $LiBH_4$ and $Li(BH)_3$ as host materials for hydrogen storage*, Eur. Phys. J. B 97 (1) (2024) 9.
[28] D.P. Broom, Hydrogen Storage Materials; the Characterisation of Their Storage Properties, 1 ed., Springer-Verlag London, 2011.
[29] S. Al, M. Yortanlı, E. Mete, *Lithium metal hydrides (Li_2CaH_4 and Li_2SrH_4) for hydrogen storage; mechanical, electronic and optical properties*, Int. J. Hydrogen Energy 45 (38) (2020) 18782–18788.
[30] Q. Zeng, et al., *Evaluation of the thermodynamic data of CH_3SiCl_3 based on Quantum chemistry calculations*, J. Phys. Chem. Ref. Data 35 (3) (2006) 1385–1390.
[31] M.M. Hossain, A. Al Mahmud, *Structural, elastic, electronic and optical properties of lead free $ZnMO_3$ (M = Ge, Sn) perovskites from first principles investigation*, Computational Condensed Matter 32 (2022) e00695.
[32] M.M. Hossain, et al., *Origin of high hardness and optoelectronic and thermo-physical properties of boron-rich compounds B_6X (X = S, Se): a comprehensive study via DFT approach*, J. Appl. Phys. 129 (17) (2021).
[33] N. Arıkan, et al., A first-principle study of Os-based compounds: electronic structure and vibrational properties, J. Phys. Chem. Solid. 96–97 (2016) 121–127.
[34] S. Al, *Investigations of physical properties of $XTiH_3$ and implications for solid State hydrogen storage*, Zeitschrift für Naturforschung A. (2019) 1023.
[35] D.G. Pettifor, Theoretical predictions of structure and related properties of intermetallics, Mater. Sci. Technol. 8 (4) (1992) 345–349.
[36] I.N. Frantsevich, F.F. V, S.A. Bokuta, in: I.N. Frantsevich (Ed.), Elastic Constants and Elastic Moduli of Metals and Insulators, Naukova Dumka, Kiev, 1983.
[37] M.A. Hadi, et al., *Mechanical behavior, bonding nature and defect processes of Mo_2ScAlC_2: a new ordered MAX phase*, J. Alloys Compd. 724 (2017) 1167–1175.
[38] A. Savin, et al., On the bonding in carbosilanes, Angew Chem. Int. Ed. Engl. 31 (2) (1992) 185–187.
[39] M.I. Naher, M.A. Afzal, S.H. Naqib, *A comprehensive DFT based insights into the physical properties of tetragonal superconducting Mo_5PB_2*, Results Phys. 28 (2021) 104612.

[40] L. Kleinman, Deformation potentials in silicon. I. Uniaxial strain, Phys. Rev. 128 (6) (1962) 2614–2621.
[41] M.A. Ali, et al., *Ternary boride Hf_3PB_4: insights into the physical properties of the hardest possible boride MAX phase*, J. Alloys Compd. 857 (2021) 158264.
[42] H. Chen, L. Yang, J. Long, First-principles investigation of the elastic, Vickers hardness and thermodynamic properties of Al–Cu intermetallic compounds, Superlattice. Microst. 79 (2015) 156–165.
[43] Y. Tian, B. Xu, Z. Zhao, Microscopic theory of hardness and design of novel superhard crystals, Int. J. Refract. Metals Hard Mater. 33 (2012) 93–106.
[44] N. Miao, et al., Theoretical investigation on the transition-metal borides with Ta3B4-type structure: a class of hard and refractory materials, Comput. Mater. Sci. 50 (4) (2011) 1559–1566.
[45] D.M.J.M.b. Teter, Computational alchemy: the search for new superhard materials 23 (1) (1998) 22–27.
[46] E. Mazhnik, A.R. Oganov, A model of hardness and fracture toughness of solids, J. Appl. Phys. 126 (12) (2019).
[47] F. Rahman, et al., *DFT approach into the physical properties of MTe_3 (M = Hf, Zr) superconductors: a comprehensive study*, AIP Adv. 13 (8) (2023).
[48] M. Mahamudujjaman, et al., *First-principles insights into mechanical, optoelectronic, and thermo-physical properties of transition metal dichalcogenides ZrX_2 (X = S, Se, and Te)*, AIP Adv. 12 (2) (2022).
[49] M. Abdellaoui, et al., *Enhancing of hydrogen storage properties of perovskite-type $MgNiH_3$ by introducing cobalt dopant ($MgCo_xNi_{1-x}H_3$) using first-principle calculations*, Appl. Phys. A 125 (11) (2019) 760.
[50] Š. Masys, V. Jonauskas, *Elastic properties of rhombohedral, cubic, and monoclinic phases of $LaNiO_3$ by first principles calculations*, Comput. Mater. Sci. 108 (2015) 153–159.
[51] Ç. Yamçıçıer, *Exploring the structural, elastic, phonon, optoelectronics, and thermoelectric properties of tetragonal complex metal hydride X_2MgH_4 (X=K, Rb, and Cs) compounds for hydrogen storage applications*, Int. J. Hydrogen Energy 48 (100) (2023) 39930–39943.
[52] Y.C. Lin, et al., *Effects of pressure on anisotropic elastic properties and minimum thermal conductivity of DO_{22}-Ni_3Nb phase: First-principles calculations*, J. Alloys Compd. 688 (2016) 285–293.
[53] J. Ju, et al., *First-principles investigations of the stability, electronic structures, mechanical properties and thermodynamic properties of $Fe_xAl_yC_z$ compounds in Fe-Cr-B-Al-C alloy*, J. Phys. Chem. Solid. 143 (2020) 109366.
[54] S. Yamçıçıer, *First-principles investigation of structural, elastic, anisotropic, dynamic, electronic, thermo-physical, and optical properties of two-dimensional trigonal M_2N (M = V, Nb, Ta) compounds for advanced technological applications*, Phys. B Condens. Matter 704 (2025) 417070.
[55] V.N. Belomestnykh, E.P. Tesleva, Interrelation between anharmonicity and lateral strain in quasi-isotropic polycrystalline solids, J Technical physics 49 (8) (2004).
[56] S.I. Mikitishin, Interrelationship of Poisson's ratio with other characteristics of pure metals, Sov. Mater. Sci. 18 (3) (1982) 262–265.
[57] X. Zhan, et al., *Theoretical prediction of elastic stiffness and minimum lattice thermal conductivity of $Y_3Al_5O_{12}$, $YAlO_3$ and $Y_4Al_2O_9$*, J. Am. Ceram. Soc. 95 (4) (2012) 1429–1434.
[58] D.R. Clarke, Materials selection guidelines for low thermal conductivity thermal barrier coatings, Surf. Coating. Technol. 163–164 (2003) 67–74.